ENCLOSURE 5

MFN 09-266

GENE-0000-0095-4020-R1-NP

Marathon Control Rod Post-Irradiation Examination (PIE)

Non-Proprietary Version

IMPORTANT NOTICE

This is a non-proprietary version of GENE-0000-0095-4020-R1-P, which has the proprietary information removed. Portions of the document that have been removed are indicated by white space with an open and closed bracket as shown here [[ ]].

HITACHI

GE Hitachi Nuclear Energy

GENE-0000-0095-4020-R1-NP
Class I
April 2009

Marathon Control Rod
Post-Irradiation Examination (PIE)

Copyright 2009 GE-Hitachi Nuclear Energy Americas LLC

INFORMATION NOTICE

This is a non-proprietary version of GENE-0000-0095-4020-R1-P, which has the proprietary information removed. Portions of the document that have been removed are indicated by whitespace with an open and closed bracket as shown here [[ ]].

IMPORTANT NOTICE REGARDING CONTENTS OF THIS REPORT

Please Read Carefully

The use of this information by anyone other than the NRC or for any purpose other than that for which it is intended, is not authorized; and, with respect to any unauthorized use, GEH makes no representation or warranty, express or implied, and assumes no liability as to the completeness, accuracy, or usefulness of the information contained in this document, or that its use may not infringe privately owned rights.

TABLE OF CONTENTS

1. INTRODUCTION 1
1.1 Purpose 1
1.2 Background 1
1.3 Marathon Control Rod Description 2
1.3.1 Mechanical Design 2
1.3.2 304S Radiation Resistant Stainless Steel 5
2. VISUAL EXAMINATION 7
2.1 Purpose 7
2.2 Results 7
2.3 Conclusions 11
3. OPTICAL METALLOGRAPHY AND SCANNING ELECTRON MICROSCOPE (SEM) MICROSCOPY 12
3.1 Purpose 12
3.2 Results 12
3.3 Conclusions 14
4. BORON CARBIDE DEPLETION ANALYSIS 15
4.1 Purpose 15
4.2 Description 15
4.3 Results 15
4.4 Conclusions 19
5. MECHANICAL PROPERTIES 20
5.1 Purpose 20
5.2 Description 20
5.3 Results 22
5.3.1 Tensile Data 22

5.3.2 Hardness Data 26
5.4 Conclusions 28
6. DIMENSIONAL MEASUREMENTS 29
6.1 Purpose 29
6.2 Description 29
6.3 Results 30
6.4 Conclusions 33
7. NEUTRON RADIOGRAPHY 34
7.1 Purpose 34
7.2 Description 34
7.3 Results 37
7.4 Conclusions 40
8. ABSORBER TUBE GAS PRESSURE ANALYSIS 41
8.1 Purpose 41
8.2 Description 41
8.3 Results 41
8.4 Conclusions 42
9. ROOT CAUSE ANALYSIS 43
9.1 Background 43
9.2 Conclusions 44
10. MARATHON DESIGN AND MANUFACTURING CHANGES 46
10.1 Marathon Weld Sequence and Absorber Tube Manufacturing 46
10.2 Square Absorber Tube Geometry Modification 46
10.3 Marathon-5S Control Rod Assembly 47
11. REFERENCES 49

1. INTRODUCTION

1.1 Purpose

This report summarizes the Post-Irradiation Examination of a high depletion Marathon control rod. Included in the examination is an investigation into the root cause of observed crack indications, the collection of irradiated property data for GEH type 304S stainless steel, and the evaluation of irradiated boron carbide swelling rates.

1.2 Background

The GEH Marathon control rod assembly was licensing by NRC in 1991 in Reference 1. Also in 1991, twenty-five (25) Marathon control rods were shipped to a domestic BWR/4. These control rods were some of the first Marathon control rods manufactured, and were periodically inspected as the lead use Marathon control rods as part of the Marathon surveillance program. A summary of the surveillance program is contained in Reference 2, which identifies this BWR/4 as “Plant A”. As shown in Reference 2, during an August 2005 inspection at Plant A, [[ ]] control rods inspected displayed crack indications. Control rod serial number 006 was selected to undergo a Post-Irradiation Examination (PIE) at Idaho National Labs with further analysis at Vallecitos Nuclear Center (VNC). Serial number 006 was selected for study because it displayed two indications on separate wings.

The full-length control rod was shipped to Idaho National Labs (INL) where a saw was designed and built to remove the individual wings from the tie rods. After two wings were removed, one wing was cut axially into four pieces and shipped to the GEH Vallecitos Nuclear Center (VNC) for examination and the other wing remained at INL for study.

Figure 1.2-1 shows a photograph through the hot cell window showing a control rod wing, just after removal from the remainder of the control rod. The other two wings are perpendicular to the plane of the photograph containing face A that is the serial number side of the control rod.

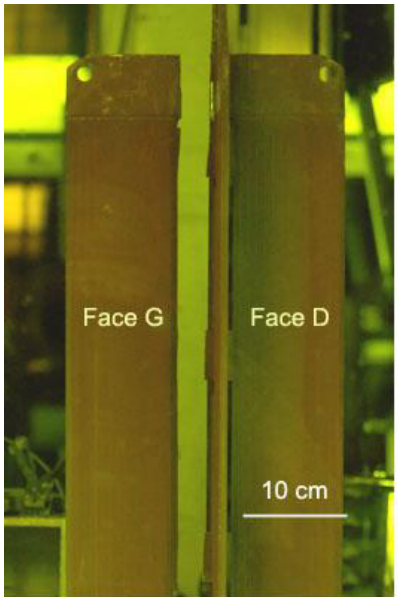

Figure1.2-1: Marathon Control Rod in the Hot Cell

1.3 Marathon Control Rod Description

1.3.1 Mechanical Design

As described in Reference 1, the marathon control rod consists of 'square' absorber tubes, edge welded together to form the control rod wings (Figure 1.3.1-1). The 'lobes' of the square absorber tubes provide both welding surface area and act as a wear surface. The four wings are welded to central tie rod segments to form a cruciform shape. A cross-sectional view of the control rod absorber section is shown in Figure 1.3.1-1.

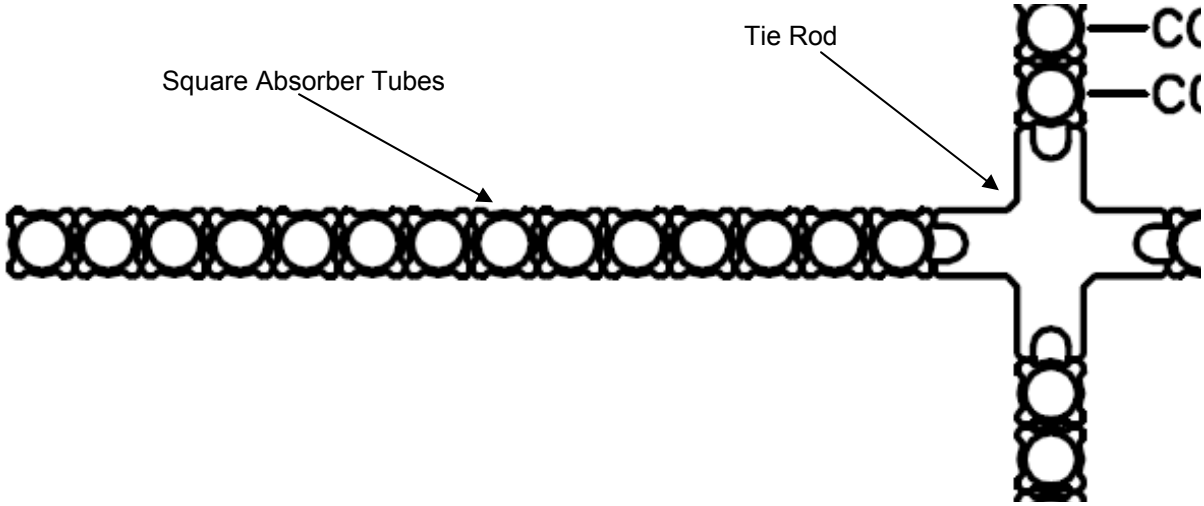

Figure 1.3.1-1: Marathon Control Rod Cross-Section

The square absorber tubes are filled with capsules containing compacted boron carbide powder, empty capsule plenums, or hafnium rods. The examined control rod is a 'D' lattice load pattern, shown in Figure 1.3.1-2. As shown in Figure 1.3.1-3, the boron carbide capsules are sized to allow a diametral gap between the capsules and the absorber tubes to allow for irradiation-induced swelling of the capsules, and to provide a volume to accommodate irradiation-generated helium gas. A large diametral gap is also provided between the hafnium rods and the absorber tubes. All absorber contents are sealed within the absorber tubes by welded end plugs.

[[

]]

Figure 1.3.1-2: Examined Marathon Control Rod Load Pattern

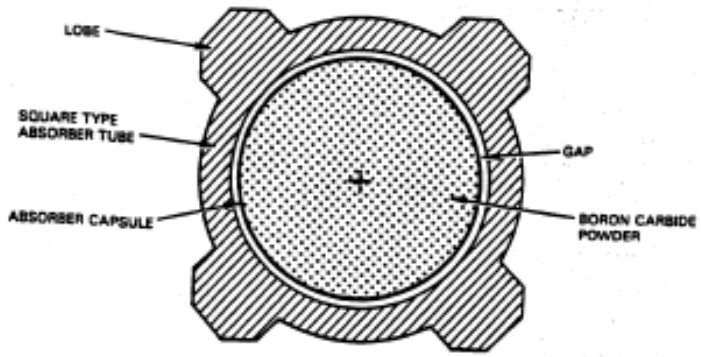

Figure 1.3.1-3: Cross-Section of Absorber Tube and Boron Carbide Capsule

A handle and velocity limiter are attached at the top and bottom respectively to complete the assembly (Figure 1.3.1-4).

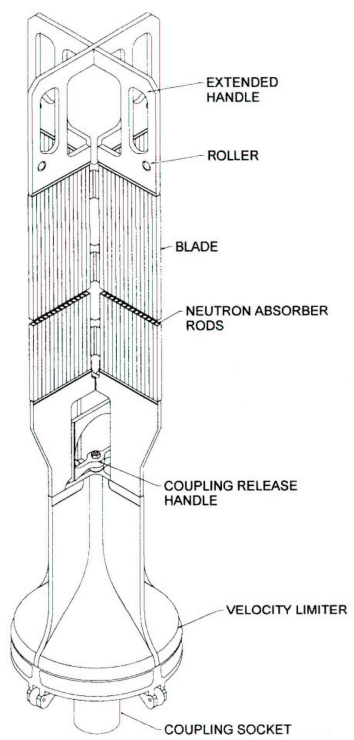

Figure 1.3.1-4: Completed Marathon Control Rod Assembly

1.3.2 304S Radiation Resistant Stainless Steel

The Marathon absorber tubes are made from GEH proprietary 'Type 304S' stainless steel. This radiation resistant stainless steel is similar to 304L stainless steel, in that they are both austenitic. Differences arise primarily from lower cobalt and reduced tramp elements. An extensive internal program was undertaken to determine the optimum composition that would resist Irradiation Assisted Stress Corrosion Cracking (IASCC). These results were used to define this alloy and were ultimately patented.

For Type 304S stainless steel, the minimum chromium level is increased from [[ ]] atomic weight percent. Chromium forms the passive film that gives stainless steel its corrosion resistance. It has been shown that there is a direct correlation between fluence and chromium depletion at the grain boundaries (Reference 4). The Nickel minimum is increased from [[ ]] atomic weight percent to help stabilize the austenitic structure and promotes reforming the passive film. Tantalum is added to Type 304S with a maximum of [[ ]] atomic weight percent and a minimum of [[ ]]. This stabilizes the austenite and inhibits the formation of chromium carbides that lower the local corrosion resistance of the metal. There is also the ability to add niobium up to [[ ]] atomic weight percent to provide additional stabilization effects.

Cobalt is controlled to a limit of 0.030 atomic weight percent to lower the increased dose from reactor coolant caused by the formation of radioactive isotopes produced from cobalt neutron interactions. Impurities like phosphorus and sulfur are reduced by about an order of magnitude from 0.045 and 0.030 atomic weight percent to 0.005 and 0.004 atomic weight percent respectively. The Silicon maximum concentration is reduced from 0.45 to 0.03 atomic weight percent. Radiation induced segregation in 300 series alloys has shown that silicon and phosphorus diffuse toward grain boundaries thus helping to contribute to an altered metallurgical state in the grain boundaries of the material. Additional impurity elements including: aluminum, boron, bismuth, tin, arsenic, lead, selenium, and antimony are also controlled to low levels in the radiation resistant 304S stainless steel. The use of high purity stainless steel has been shown to be beneficial to stress corrosion cracking resistance.

The bases of the improved performance when subjected to irradiation are the following:

- [[

]]

Given the operating environment of the control rod blade, Irradiation Assisted Stress Corrosion Cracking (IASCC) is the failure mechanism of greatest concern for the absorber section. For IASCC to occur the material must be irradiated, susceptible, exposed to a conducive environment and be subjected to an applied stress either mechanically induced or residual.

2. VISUAL EXAMINATION

2.1 Purpose

A thorough visual examination was performed documenting the as-received condition of the control rod and to provide traceability after disassembly. Figure 2.1-1 shows a schematic of the control rod indicating the wing-labeling scheme with reference to the control rod's serial number face.

[[

]]

Figure 2.1-1: Control Rod Wing Side Labeling

2.2 Results

The initial visual exam conducted at INL indicated that wings containing sides C and H had cracks in the second tube as measured from the tie rod (Figure 2.1-1). The crack indications were measured and photographed. [[

]]

[[ ]]

Figure 2.2-1: Marathon Control Rod S/N 0006 Showing Two Indications on Wing Side H

The locations of the crack indications were primarily in the transition radius of the square absorber tube (Figure 2.2-2). Occasionally, the long crack transferred from one transition radius to the other, typically within the same tube. The cracks did not visually propagate into the welds joining the absorber tubes. For the entire visual inspection, none of the crack indications were observed in the laser welds that join the square absorber tubes, but water was found in tube 1 of wing C at INL during disassembly when the saw inadvertently cut into tube one (Figure 2.2-3).

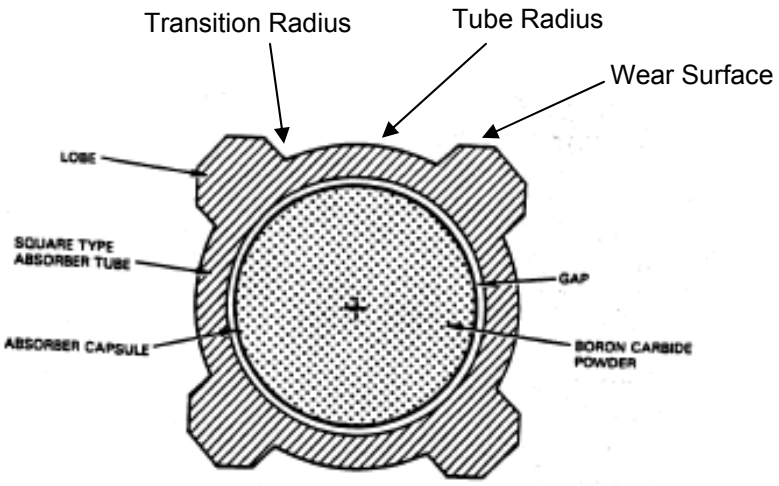

Figure 2.2-2: Square Absorber Tube Geometry

[[

]]

Figure 2.2-3: Saw Blade Cut Into Tube 1 at INL where Water Discharged

The lack of observed cracks in the laser welds suggests that the weld heat affected zone (HAZ) was not sensitized and did not initiate the cracking. This indicates that the laser welding process, and the resulting residual stress from joining the square absorber tubes is not the driving force for the crack indications. The general appearance of the cracks is jagged in nature, which suggests the cracks are intergranular and is consistent with Irradiation Assisted Stress Corrosion Cracking (IASCC).

2.3 Conclusions

The lack of visual cracking adjacent to the laser welds indicates that weld sensitization did not play a role in crack initiation. The cracks appear to remain within a single tube, and do not generally propagate into, nor initiate in the weld joining the absorber tubes. [[

]]

3. OPTICAL METALLOGRAPHY AND SCANNING ELECTRON MICROSCOPE (SEM) MICROSCOPY

3.1 Purpose

The nature of the IASCC propagation mechanism correlates it closely with low stress grain boundary failure of the affected material. To confirm the intergranular nature of the cracks, a series of metallographic mounts were cut and prepared for optical microscopy and SEM analysis.

3.2 Results

Figure 3.2-1 shows an intergranular crack with smaller crack offshoots, which is consistent with IASCC. The crack/corrosion follows the stress profile contained within the metal. Since it is dependent on the residual strain, the crack moves around the grains until the stress orientation causes it to no longer be above the growth threshold. This effectively shuts off the crack's progress as grain boundaries that are properly oriented to the stress field continue to grow cracks. Eventually the path with grain orientations most favorable to crack growth surpasses the others and becomes continuous (Figure 3.2-1). Figure 3.2-2 shows a 100x view of the fracture surface indicating both grain separation and intergranular propagation that is associated with IASCC.

[[

]]

Figure 3.2-1: Optical Micrograph of Intergranular Crack on Wing Side H at VNC

[[

]]

Figure 3.2.2: 100x SEM Photograph Taken on the Top, Left Side of the Fracture Surface

3.3 Conclusions

The optical micrographs and SEM pictures collected at both INL and VNC on the two wings evaluated are consistent with Irradiation Assisted Stress Corrosion Cracking (IASCC)

4. BORON CARBIDE DEPLETION ANALYSIS

4.1 Purpose

The purpose of performing a chemical depletion analysis is to determine a more accurate Boron Carbide (B_4C) depletion at specific areas of the control rod. This data was then compared to the depletion data from the plant process computer. This data is used to determine the relative depletion/fluence levels at areas where mechanical properties data was collected.

4.2 Description

ASTM standard C 791-04 for ^{10}B depletion was adhered to for both the data collected at VNC and INL. The bulk of the data was collected at INL with three samples run at VNC as a reference check. The basis for the calculation of ^{10}B is:

$$D = 100 \cdot [1-(^{10}B/^{11}B) \cdot S],$$

where D is ^{10}B depletion in percent and S is the $^{10}B/^{11}B$ ratio of a Boron Carbide poison sample prior to irradiation exposure.

4.3 Results

Table 4.3-1 shows a map of expected ^{10}B percent depletions based on nodal depletions from the plant process computer, and a radial profile from the nuclear analysis. Table 4.3-2 shows measured Boron-10 percent depletions based on the chemical analysis described above. Finally, Table 4.3-3 shows a ratio of measured depletion values to depletion values from the plant process computer. As shown, there is a good correlation between the measured values and the process computer values, with the measured values being slightly higher. For most locations, the measured values are within 10% of the process computer values.

[[

]]

Table 4.3-1: Local 10B Depletion Map Based on Plant Process Computer (Each Node Represents 6 Linear Inches)

[[															
				--		---			---		--	--			
								--			--	--			
										--		--			
												--			
				--								---------- --------			
															]]

Table 4.3-2: Local Depletion Data in Percent Depletion of ^{10}B

[[															
															]]

Table 4.3-3: Local Depletion Data in Percent Depletion of ^{10}B vs. plant supplied measured data

4.4 Conclusions

Tube #11 contains the area of highest interest due to the larger local depletions that were feasible to measure. Tube #2 contained the crack [[
]]. There is good correlation between the plant supplied data and the measured data, with the measured depletion data being consistently slightly higher (Table 4.3-3) than the plant data. For practical purposes the plant-generated data will be used for relevant correlations contained within the discussion section of this paper.

5. MECHANICAL PROPERTIES

5.1 Purpose

Given the limited amount of irradiation data, samples were removed to obtain materials properties data on Type 304S.

5.2 Description

Tensile test data provides insight into how a metal will behave under given service conditions. It provides ultimate tensile strengths, 2% offset yield strength and elongation data at a given temperature for the bulk material. Hardness data provides a relative measure of a metal's resistance to surface abrasion and is an indirect measure of metal's ductility. Typically, as a metal's hardness increases its ductility decreases. This is the case with irradiated type 304S and this test is used to provide a relative measure of the metal's irradiation induced damage at a given ^{10}B depletion. Six samples from three different locations were chosen to perform tensile testing (Figure 5.2-1 and 5.2-2).

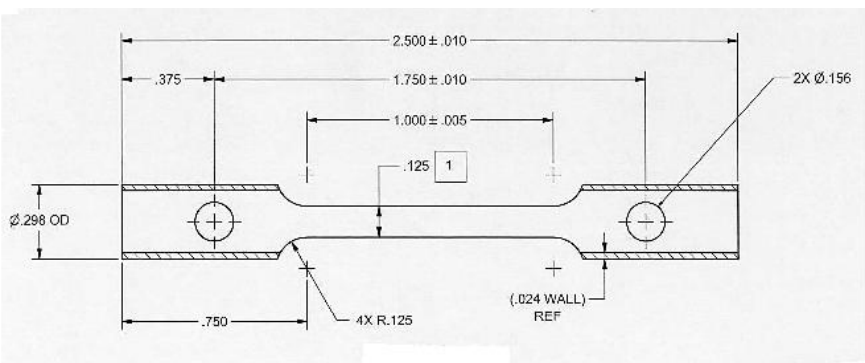

Figure 5.2-1: Tensile Sample Dimensions

[[

]]

Figure 5.2-2 Sampling Plan for SEM, Micrographs, Dosimetry and Tensile Testing

5.3 Results

5.3.1 Tensile Data

Six samples were tensile tested at both at room temperature (~70 °F) and at in-service conditions (550 °F / 288 °C) from the [[ ]] depletion area (Figure 5.2-2). Sample stress-strain plots are shown in Figures 5.3.1-1 through 5.3.1-5.

[[

]]

Figure 5.3.1-1 Tensile Stress vs. Strain for Sample 30149 at Room Temperature.

[[

]]

Figure 5.3.1-2 Tensile Stress vs. Strain for Sample 30149 at 288 °C.

[[

]]

Figure 5.3.1-3 Tensile Stress vs. Strain for Sample 30150 at Room Temperature.

[[

]]

Figure 5.3.1-4 Tensile Stress vs. Strain for Sample 30150 at 288 °C.

[[

]]

Figure 5.3.1-5 Tensile Stress vs. Strain for Sample 30151 at Room Temperature.

[[

]]

Figure 5.3.1-5 Tensile Stress vs. Strain for Sample 30151 at 288 °C.

It is well known that stainless steel, when irradiated loses some ductility. In general, as the material is irradiated, the yield and ultimate strengths of the metal increase due to irradiation-hardening. At the same time, the total elongation or ultimate strain of the material is reduced.

The tensile tests shown in Figures 5.3.1.1 through 5.3.1.5 are consistent with Type 304S stainless steel at this amount of irradiation. Of most significance, the plots demonstrate that some ductility remains in the irradiated material. For the plots at plant operating temperatures, a [[ ]] average elongation is demonstrated.

5.3.2 Hardness Data

Figure 5.3.2-1 plots Knoop harness verses plant generated depletion data and shows no correlation. As shown, the average hardness of the 304S at the fracture is [[ ]] yet the average hardness in tube 10 where no fracture exists is [[ ]] indicating that there is no direct correlation between the hardness of the stainless steel and crack initiation susceptibility.

[[

]]

Figure 5.3.2-1 Knoop hardness verses Depletion

[[

]]

Table 5.3.2-1: Knoop Hardness Data at Specifications on the Control Rod

5.4 Conclusions

The tensile tests are consistent with Type 304S irradiated material behavior. The test data demonstrates a ductility of approximately [[ ]] at operating reactor conditions.

The hardness data indicates that there is no apparent correlation between material hardness and crack susceptibility. There is also no apparent correlation between hardness and depletion either.

6. DIMENSIONAL MEASUREMENTS

6.1 Purpose

Dimensional measurements of the irradiated control rod were performed to evaluate boron carbide swelling as a function of Boron-10 depletion.

As boron carbide powder is irradiated, a swelling phenomenon occurs. The neutron capture reaction with Boron-10 produces a helium atom. Some of this helium is released as a gas, with the remaining helium trapped within the compacted boron carbide powder matrix. This results in a diametral swelling of the cylindrical column of compacted boron carbide powder. The design basis for GEH control rods uses data collected from a controlled experiment in which test boron carbide filled capsules were irradiated, with dimensional measurements taken before and after the test. Dimensional data from the irradiated Marathon control rod is compared to the design basis.

6.2 Description

Paragraph 3.6.1 of Reference 3 contains a description of the test that produced the design basis boron carbide swelling rates. As discussed, this data shows a nominal diametral swelling of [[ ]] at 100% local Boron-10 depletion, with a +3σ upper bound of [[ ]].

As part of the Marathon control rod examination, a micrometer was used to measure the outside diameter of the round portion of the square absorber tubes, as shown in Figure 6.2-1. Locations chosen for the diametral measurement focused on high depletion portions of the control rod wing. Measurements were also made at baseline locations at the bottom of the absorber section, as well as in the outer 3 absorber tubes that contain hafnium rods, and the first absorber tube that is empty (see Figure 1.3.1-2). This was done as a comparison as these locations are not subject to the effects of boron carbide swelling. The locations at the bottom of the absorber section have very low Boron-10 depletions, and are not subject to boron carbide swelling. Since there is a large diametral gap between the hafnium rod and the absorber tube inside diameter, the tubes containing hafnium rods are not expected to experience swelling strain. Likewise, the first, empty tube is not expected to experience diametral swelling.

Since the examined control rod was not part of a controlled experiment in which precise dimensions were recorded prior to irradiation, several assumptions were made. Specifically, it is assumed that all beginning of dimensions were at absorber tube and capsule body tube drawing nominal values, and an apparent measurement error offset is corrected based on unstrained tube measurement baseline locations. Based on these assumptions, the diametral strain of the boron carbide powder column is calculated. These diametral strains can then be compared to Boron-10 depletion measurements, taken from the same control rod (See Section 4).

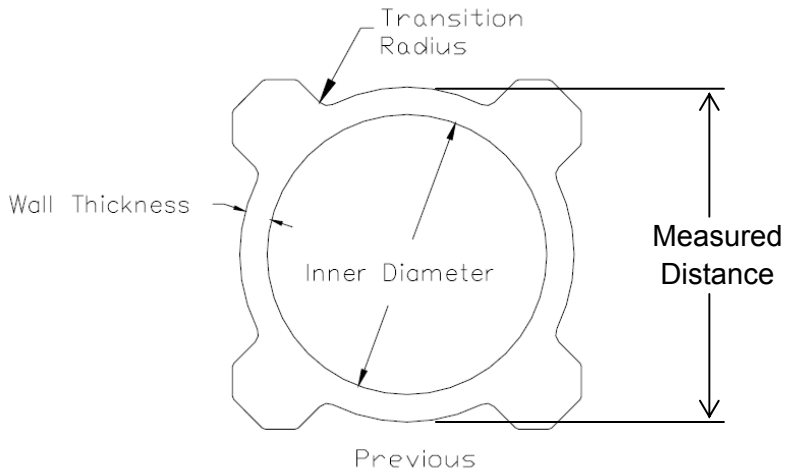

Figure 6.2-1: Square Tube Geometry and Measurement Location

6.3 Results

Figure 6.3-1 shows the previously available 'Experiment' data, and the new 'Marathon' diametral swelling data, plotted against percent local Boron-10 depletion. Also plotted on this graph are design basis nominal ([[ ]]) and +3σ upper bound ([[ ]]) boron carbide swelling lines. [[
]]

[[

]]

Figure 6.3-1: Boron Carbide Swelling versus Percent Boron-10 Depletion

The data plot in Figure 6.3-1 supports the assumed linear relationship between swelling and percent depletion. Furthermore, all data points are bound by the +3σ upper limit.

The swelling data is then normalized to 100% local depletion, assuming the linear relationship. Statistical summaries are presented below for the Experimental data, and the new Marathon data. As shown, the new Marathon data closely matches the Experimental data, with a slightly higher mean, with a slightly lower standard deviation.

[[

]]

Figure 6.3-2: Experimental Swelling Data Summary

[[

]]

Figure 6.3-3: Marathon Swelling Data Summary

A one-way ANOVA is performed to evaluate if the two data sets are different. As shown by a high P-value of 0.648, the test does not suggest that the data sets are different. Therefore, a combined data set, shown below, may also be used.

One-way Analysis of Variance

[[

]]

Figure 6.3-4: One-Way Analysis of Variance

[[

]]

Figure 6.3-5: Combined Swelling Data Summary

A final summary of +3σ upper limit boron carbide swelling rates for the various data sets is shown below. As shown, both the values for the new Marathon data alone, or a combined data set are bound by the design basis value of [[ ]] diametral swelling at 100% local Boron-10 depletion.

Data Set	Boron Carbide Swelling, +3σ Upper Limit
Experimental Data (Design Basis)	[[
Marathon Data (from PIE)	
Combined Data	]]

Table 6.3-1: Boron Carbide Swelling +3σ Upper Limit

6.4 Conclusions

The dimensional measurements taken from the irradiated Marathon control rod strongly support the design basis boron carbide swelling rates of [[ ]] nominal, [[ ]] +3σ upper limit. The new data very closely matches the existing data, and supports the assumed linear relationship between swelling and percent Boron-10 depletion. All available data is bound by the [[ ]] upper limit.

7. NEUTRON RADIOGRAPHY

7.1 Purpose

Neutron Radiography was performed at INL to evaluate the general condition of the neutron absorber in the control rod. Particular attention was paid to the effect of water infiltration in cracked tubes with respect to how the water affected the compacted boron carbide powder within the absorber capsules.

7.2 Description

Two sets of Neutron Radiograph images were made of wing C; one using dysprosium (Dy) foil and one with indium (In) foil to expose the films. The foils absorb neutrons at different energy levels and therefore have different resolutions and depth penetrations. The Dy foil is activated by thermal neutrons while the In foil is activated by higher energy epithermal neutrons. The neutrons were provided by the TRIGA reactor located at the INL facility. A test sample was developed at GEH that was used both as a reference and to help INL determine optimum exposure times. The contents of the 14 absorber tubes in the reference sample is shown in Table 7.2-1. A Neutron Radiograph of the reference sample with Dy foil activation is shown in Figure 7.2-1. Note that the horizontal red line indicates the picture overlap break.

Tube No.	Materials	Comments
1	hafnium	
2	B_4C	Standard mix of three particle sizes - dry
3	B_4C	Finer than 200 mesh – tapped only to pack - dry
4	B_4C	20/40 mesh – dry
5	B_4C	60/80 mesh – dry
6	B_4C	200/280 mesh – dry
7	B_4C - water	Longitudinal slit in inner tube, thump to pack, fill with water*
8	B_4C – water	Longitudinal slit in inner tube, thump to pack, fill with water*
9	B_4C – water	Large hole in inner tube, thump to pack, fill with water*
10	B_4C – water	Free volume (1/2 of tube) 100% filled with water
11	B_4C – water	Free volume (1/2 of tube) 3/4 filled with water, ~11.7 cc water
12	B_4C – water	Free volume (1/2 of tube) 1/2 filled with water, ~7.8 cc water
13	B_4C – water	Free volume (1/2 of tube) ¼ filled with water, ~3.9 cc water
14	water	*Water added at the INL site

Table 7.2-1: Contents of the Neutron Radiography Reference Sample

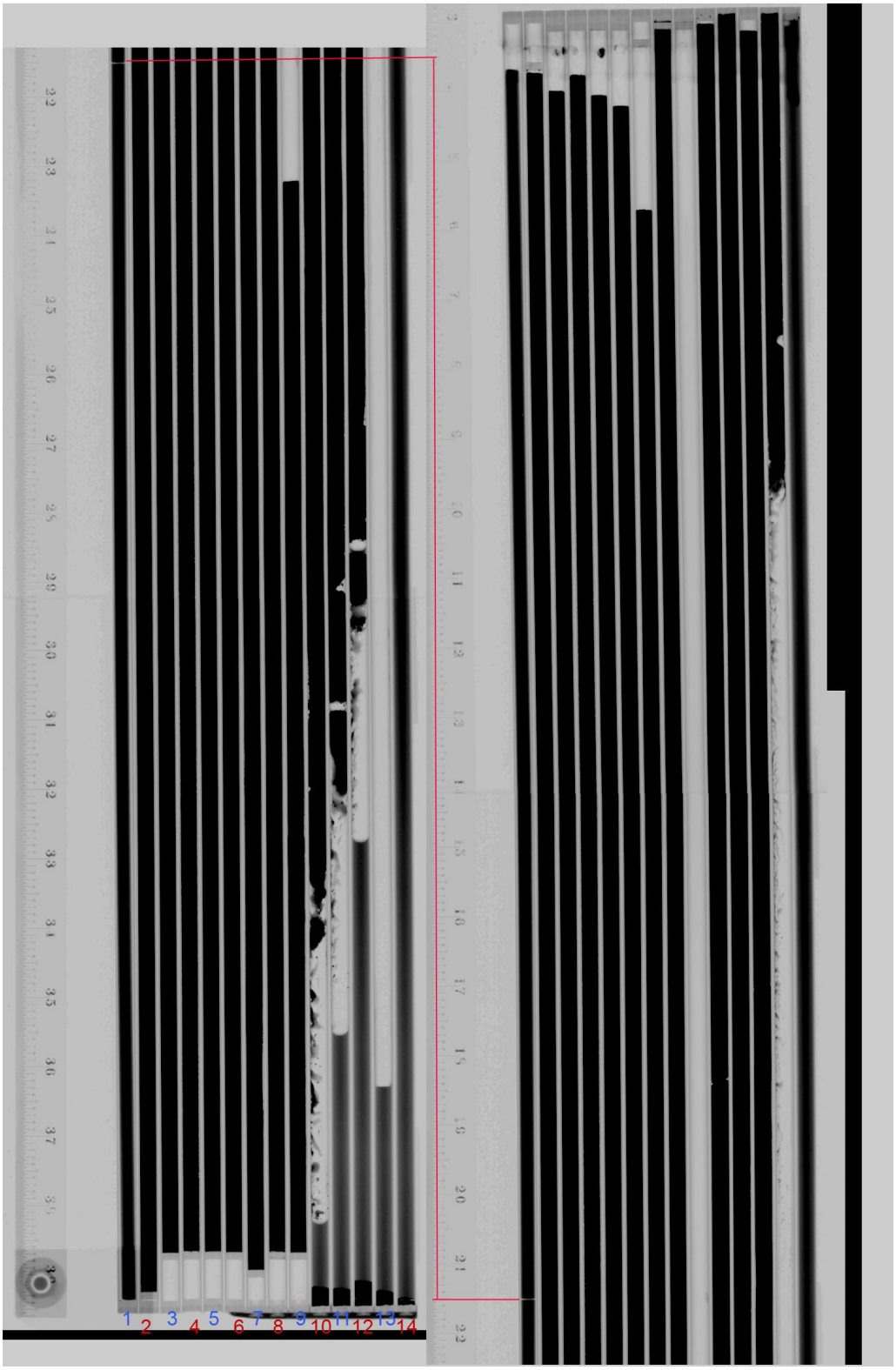

Figure 7.2-1: Neutron Radiograph of Reference Sample

7.3 Results

[[

]]

[[

]]

Figure 7.3-1 Thermal Neutron Radiograph [[

]]

[[

]]

[[

]]

Figure 7.3-2: Neutron Radiography Montage [[

]]

[[

]]

[[

]]

Figure 7.3-3: Neutron radiography montage [[

]]

[[

]]

[[

]]

Figure 7.3-4: [[

]]

7.4 Conclusions

The majority of the crack length is confined to the transition radius and is intergranular. [[

]]

8. ABSORBER TUBE GAS PRESSURE ANALYSIS

8.1 Purpose

Internal pressure measurements are taken from two square absorber tubes to evaluate the pressurization methodology used for Marathon control rod design.

As boron carbide powder is irradiated, the neutron capture reaction with Boron-10 produces a helium atom. Some of this helium is trapped within the boron carbide powder matrix, resulting in the swelling phenomenon evaluated in Section 6 of this report. The remaining helium is released as a gas. The crimped end cap connection of the Marathon capsule is designed to allow this helium gas to escape, and fill the volume between the capsule and the outer absorber tube, thereby pressurizing the outer absorber tube.

The methodology GEH uses to predict helium generation and absorber tube pressurization is described in Sections 3.6 and 4.6 of Reference 3. [[

]] Using this relationship, the mechanical lifetime limit of each absorber tube, and the control rod assembly is determined.

8.2 Description

The hot cell laboratory used for this investigation is equipped with a gas collection system that is capable of measuring the pressure of enclosed volumes, such as the sealed Marathon absorber tubes. The apparatus consists of a gas collection system in which standard volumes are attached to the collection system and a temporary seal is made between the sampling device and the sample tube. A window is part of the sealing hardware that allows a laser to be fired onto the sample surface, puncturing the tube.

The gas is released from the absorber tube and collected in a standard volume, where its pressure is measured. By using a procedure in which the absorber tube is back-filled to a series of prescribed pressures, the volume and pressure inside the absorber tube prior to the tube puncture may be determined.

8.3 Results

The internal pressures of two absorber tubes were measured: that of uncracked tube #4 and tube #11. The measured pressures are shown in Table 8.3-1. The predicted pressures in these tubes, based on the depletions shown in Table 4.3-1 and the methodology described in Section 8.1, are shown in Table 8.3-1 for comparison. Note that the pressurization methodology predicts the tube pressure at operating temperature. Since the test was performed at room temperature, the operating temperature pressures were scaled to room temperature using the ideal gas law.

Case	Predicted Pressure at Operating Temperature (psia)	Predicted Pressure at Room Temperature (psia)	Measured Pressure (psia)
Tube # 4	[[		
Tube # 11			]]

Table 8.3-1: Absorber Tube Internal Pressure – Predicted Versus Measured

8.4 Conclusions

As shown in Table 8.3-1, the measured pressures inside the square absorber tubes were much less than predicted. This indicates that GEH's pressurization methodology, including the helium release fraction design basis, is very conservative. Since the pressures are very low, absorber tube pressurization is eliminated as a potential contributing factor to the observance of absorber tube cracks.

9. ROOT CAUSE ANALYSIS

9.1 Background

Irradiation Assisted Stress Corrosion Cracking (IASCC) is a dominant failure mechanism in stainless steels exposed to neutron fluence. The requirements for this failure mechanism are three-fold:

1.) Residual or Applied Tensile Stress

2.) Susceptible Material

3.) Conducive Environment

In short, by removing 1 of the three elements the threat of IASCC is mitigated. To date IASCC in absorber sections has only been documented on boron carbide containing tube sections. This has been attributed to B_4C swelling exerting pressure on the stainless steel tube. Boron carbide decomposes into Lithium (^{7}Li), Helium (^{4}He), Hydrogen (^{3}H), and Carbon (C) via the burnout of ^{10}B by one of two reactions,

$$^{10}B + n \rightarrow {}^{4}He + {}^{7}Li \qquad (1)$$

or

$$^{10}B + n \rightarrow 2\,{}^{4}He + {}^{3}H \qquad (2)$$

with reaction (1) $^{10}B + n \rightarrow {}^{4}He + {}^{7}Li$ more prevalent in the thermal neutron energy spectrum. The helium gas gets confined by the remaining boron and newly produced lithium forming gaseous bubbles (Figure 9.1-1).

[[

]]

Figure 9.1-1: 5x Magnification Photograph of Helium Gas Bubbles.

The associated volume change from solid to gas, and resulting diametral swelling of the boron carbide column, imparts a stress on the tube wall.

[[

]]

9.2 Conclusions

[[

]]

10. MARATHON DESIGN AND MANUFACTURING CHANGES

10.1 Marathon Weld Sequence and Absorber Tube Manufacturing

[[

]]

10.2 Square Absorber Tube Geometry Modification

[[

]]

[[

]]

Figure 10.2-1: D/S Lattice Square Absorber Tube Geometry Change

Finite element analysis is used to demonstrate that the new geometry meets all design requirements for maximum outer diameter strain due to capsule swelling, internal pressure, and maximum stress from loads imposed by channel bow. The new geometry is demonstrated to meet stuck rod requirements, and all control rod welds affected by the new absorber tube geometry are demonstrated to withstand loads from scram, seismic events and channel bow.

The new D/S lattice square tube geometry began implementation in 2006. All 2008 and future deliveries will use the new square absorber tube geometry. No changes have been made to the C lattice square tube design. [[

]]

10.3 Marathon-5S Control Rod Assembly

GEH has introduced the new Marathon-5S control rod design, as described by Reference 3.

[[

]]

Marathon Design	Licensing Topical Report(s)	Local Depletion at Capsule Contact with Absorber Tube Inside Diameter (Nominal)
Marathon – D/S Lattice	NEDE-31758P-A (Ref. 1)	[[
Marathon – C Lattice	NEDE-31758P-A (Ref. 1)	
Marathon-5S – D/S Lattice	NEDE-33284P Rev. 1 (Ref. 3)	
Marathon-5S – C Lattice	NEDE-33284P Rev. 1 (Ref. 3)	]]

*Nominal depletion at contact based on original square absorber tube geometry described in Section 10.2. Nominal depletion at contact for the modified D/S lattice square tube geometry is [[ ]]

Table 10.3-1: Marathon Capsule to Absorber Tube Gap Comparison

[[

]]

[[

]]

11. REFERENCES

1. GEH Licensing Topical Report: NEDE-31758P-A, “GE Marathon Control Rod Assembly”, October 1991.
2. Letter from GEH to NRC: MFN 08-355, “Marathon Control Rod Assembly Surveillance Program Update”, April, 2008.
3. GEH Licensing Topical Report: NEDE-33284P Rev. 1, “Marathon-5S Control Rod Assembly”, November 2007.
4. Was, G.S., P.L. Andresen. “ Stress Corrosion Cracking Behavior of Alloys” CORROSION 63(2007): pp. 30-40.
5. O. Gebhart and D. Gavillet, “SIMS Imaging Analyses of In-reactor Irradiated Boron Carbide Control Rod Samples,” Journal of Nuclear Materials, v. 279, issues 2-3 (2000) p.368-371.